

1 **Turbulence Measurements from Compliant Moorings - Part II: Motion**

2 **Correction**

3 Levi F. Kilcher*

4 *National Renewable Energy Laboratory, Golden, Colorado, USA*

5 Jim Thomson

6 *Applied Physics Laboratory, University of Washington, Seattle, Washington, USA*

7 Samuel Harding

8 *Pacific Northwest National Laboratory, Richland, Washington, USA*

9 Sven Nylund

10 *Nortek AS, Norway*

11 *Corresponding author address: Levi Kilcher, National Renewable Energy Laboratory, 15013 Den-
12 ver West Pkwy, Golden, Colorado, USA

13 E-mail: Levi.Kilcher@nrel.gov

ABSTRACT

14 Acoustic Doppler velocimeters (ADVs) are a valuable tool for making high-
15 precision measurements of turbulence, and moorings are a convenient and
16 ubiquitous platform for making many kinds of measurements in the ocean.
17 However, because of concerns that mooring motion can contaminate turbu-
18 lence measurements and acoustic Doppler profilers make mid-depth veloc-
19 ity measurements relatively easy, ADVs are not frequently deployed from
20 moorings. This work demonstrates that inertial motion measurements can
21 be used to reduce motion-contamination from moored ADV velocity mea-
22 surements. Three distinct mooring platforms were deployed in a tidal channel
23 with inertial-motion-sensor-equipped ADVs. In each case, motion correction
24 based on the inertial measurements reduces mooring motion contamination of
25 velocity measurements. The spectra from these measurements are consistent
26 with other measurements in tidal channels, and have a $f^{-5/3}$ slope at high
27 frequencies—consistent with Kolmogorov’s theory of isotropic turbulence.
28 Motion correction also improves estimates of cross spectra and Reynold’s
29 stresses. Comparison of turbulence dissipation with flow speed and turbu-
30 lence production indicates a bottom boundary layer production-dissipation
31 balance during ebb and flood that is consistent with the strong tidal forcing
32 at the site. These results indicate that inertial-motion-sensor-equipped ADVs
33 are a valuable new tool for making high-precision turbulence measurements
34 from moorings.

³⁵ **1. Introduction**

³⁶ Acoustic Doppler velocimeters (ADVs) have been used to make high-precision measurements of
³⁷ water velocity for over 20 years (Kraus et al. 1994; Lohrmann et al. 1995). During that time, they
³⁸ have been deployed around the world to measure turbulence from a range of platforms, including
³⁹ the laboratory setting (Voulgaris and Trowbridge 1998), from stationary structures on ocean-, river-
⁴⁰ and lake-bottoms (Kim et al. 2000; Lorke 2007; Cartwright et al. 2009), in surface waters from
⁴¹ a pole lowered from a ship's bow (Geyer et al. 2008), and in the deep ocean from autonomous
⁴² underwater vehicles (e.g., Zhang et al. 2001; Goodman et al. 2006).

⁴³ A relatively small fraction of ADV measurements have been made from moorings (e.g., Fer and
⁴⁴ Paskyabi 2014). Presumably this is because mooring motion can contaminate ADV measurements,
⁴⁵ and acoustic Doppler profilers (ADPs) can ~~be used to measure~~ measure some mid-depth turbulence
⁴⁶ statistics without a mooring (e.g., Stacey et al. 1999a; Rippeth et al. 2002; Wiles et al. 2006;
⁴⁷ Guerra Paris and Thomson 2017). Still, ADV measurements have distinct characteristics that can
⁴⁸ be advantageous: they are capable of higher sample rates, have higher signal-to-noise ratios, and
⁴⁹ have a much smaller sample volume (1 centimeter, as opposed to several meters).

⁵⁰ Inertial motion unit (IMU) sensors have been used in the aerospace and aeronautical industries
⁵¹ to quantify the motion of a wide range of systems, and to improve atmospheric velocity measure-
⁵² ments, for several decades (Axford 1968; Edson et al. 1998; Bevly 2004). In the last decade, the
⁵³ smartphone, drone, and ‘Internet of Things’ markets have driven innovation in microelectrical-
⁵⁴ mechanical systems, including the IMU. As a result of this growth and innovation, the cost, power
⁵⁵ requirements, and size of IMUs have come down. These changes have allowed these sensors to be
⁵⁶ integrated into oceanographic instruments that have small form-factors, and rely on battery power.

57 Nortek now offers a version of their Vector ADV with a Microstrain 3DM-GX3-25 IMU sensor
58 (Nortek 2005; MicroStrain 2012). This IMU's signals are incorporated into the Vector data stream
59 so that its motion and orientation signals are tightly synchronized with the ADV's velocity mea-
60 surements. ~~This~~The tight synchronization provides a dataset that can be utilized to quantify ADV
61 motion in the Earth's inertial reference frame, and remove that motion from the ADV's velocity
62 measurements at each time step of its sampling (Edson et al. 1998). This work utilizes ~~moored~~
63 'ADV-IMU' measurements from ~~mid-depths~~mid-depth moorings in Puget Sound to demonstrate
64 that motion correction can improve the accuracy of oceanic turbulence spectra, turbulence dissi-
65 pation, and Reynolds stress estimates.

66 This effort was originally motivated by a need for low-cost, high-precision turbulence measure-
67 ments for the emerging tidal energy industry (McCaffrey et al. 2015; Alexander and Hamlington
68 2015). Experience in the wind energy industry has shown that wind turbine ~~lifetime is~~lifetimes are
69 reduced by atmospheric turbulence, and the same is expected to be true for tidal energy turbines.
70 In the atmosphere, meteorological towers are often used to position sonic anemometers at the hub
71 height of wind turbines for measuring detailed turbulence inflow statistics (Hand et al. 2003; Kel-
72 ley et al. 2005; Mücke et al. 2011; Afgan et al. 2013). In the ocean, tower-mounted hub-height
73 turbulence measurements have been made, but they are challenging to install and maintain in en-
74 ergetic tidal sites (Gunawan et al. 2014; Thomson et al. 2012). Therefore, the U.S. Department
75 of Energy funded this work to investigate the accuracy of mooring-deployed ADV-IMUs to re-
76 duce the cost of turbulence measurements at tidal energy sites (Kilcher et al. 2016). The approach
77 proved to be successful and potentially useful to the broader oceanographic community interested
78 in moored turbulence measurements (Lueck and Huang 1999; Doherty et al. 1999; Nash et al.
79 2004; Perlin and Moum 2012; Alford 2010; Paskyabi and Fer 2013).

80 The next section describes details of the measurements, including a summary of the hardware
81 configurations (platforms) that were used to support and position the ADV-IMUs in the water
82 column. A detailed description of the motion of these platforms is found in the companion paper
83 to this work, [Harding et al. \(in review\)](#)[Harding et al. \(2017\)](#), hereafter Part 1. Section 3 describes
84 the mathematical details of motion correction and Section 4 presents results from applying the
85 method to measurements from the various platforms. Section 5 is a discussion of the energetics of
86 the tidal channel in which the measurements were made and demonstrates that the measurements
87 are consistent with turbulence theory and other measurements in similar regimes. A summary and
88 concluding remarks are provided in Section 6.

89 **2. Measurements**

90 This work focuses on measuring turbulence from ADVs that are equipped with IMUs and de-
91 ployed from moving (moored) platforms. The ADVs utilized for these measurements were Nortek
92 Vector ADVs equipped with Microstrain 3DM-GX3-25 [IMU sensors](#)[IMUs](#). These IMUs captured
93 all six components of ADV motion (three components of angular rotation and three components
94 of linear acceleration), as well as the orientation of the ADV pressure case. The IMU measures its
95 motion at 1 kHz and uses internal signal integration (Kalman filtering) to output the motion signals
96 at the same sample rate as the ADV's velocity measurements (the measurements are synchronized
97 to [with](#)[within](#) 10^{-2} s). This reduces aliasing of the IMU's motion measurements above the ADV's
98 sample rate (MicroStrain 2010).

99 All measurements used in this work were made in Admiralty Inlet, Washington, approximately
100 500 m west southwest of Admiralty Head in 60 m of water at $48^{\circ} 9.18' \text{ N}$, $122^{\circ} 41.22' \text{ W}$ (Fig-
101 ure 1). The site is approximately 6 km east of Port Townsend. Admiralty inlet is the largest
102 waterway connecting Puget Sound to the Strait of Juan de Fuca, and it possesses a large semid-

103urnal tidal flow (Thomson et al. 2012; Polagye and Thomson 2013). This work utilizes data
104from three distinct deployment platforms: the tidal turbulence mooring, a StableMoor buoy, and
105a sounding weight. ~~All data used in this analysis are available from the MHK data repository~~
106(<http://mhkdr.openei.org>; submission ids: 49, 50 and 51). Each of these platforms are briefly
107described below, and additional details, photos, and schematic diagrams can be found in Part 1.
108This entire work—including manuscript source text, source data, figures, and analysis scripts—are
109publicly available (Kilcher et al. 2017).

110 *a. Tidal Turbulence Mooring*

111 The tidal turbulence mooring (TTM) is a simple mooring system with a strongback fin sus-
112 pended between a steel clump-weight anchor weighing 1,200 kg when dry and a 0.93-m-diameter
113 spherical steel buoy with a buoyancy of 320 kg. The ADV pressure cases were clamped to one
114 side of the strongback fin and the ADV sensor head was positioned 10 cm in front of the fin's
115 leading edge (Figure 2). The leading edge of the fin is fastened inline with the mooring line. This
116 configuration was designed to work like a weather vane, such that the drag on the fin held the ADV
117 head upstream of the mooring components. This work utilizes data from two TTM deployments.

118 The first TTM deployment was ~~in~~from 1730 local time (LT) 12 June 2012 ~~from 17:30 on the~~
119 ~~12th until~~until 1430 LT 14 ~~:30 on the 14th (local; i.e., Pacific Daylight Time)~~. June 2012. Two
120 Nortek ADVs were clamped to either side of the fin so that the axis of their cylindrical pressure
121 cases were parallel with the leading edge of the strongback. The ADV heads were spaced 0.5 m
122 apart vertically along the fin. Only one of these ADVs was equipped with an integrated IMU. This
123 TTM also had an upward-looking ADP mounted on the mooring anchor.

124 Periods of time during which this mooring interfered with a beam of the ADP were identified
125 by inspecting the profiler's acoustic amplitude signal. Periods during which one beam of the

¹²⁶ profiler had > 5% higher acoustic amplitude than the other beams were flagged as “contaminated”
¹²⁷ and excluded from averaging. Five-minute averages in which more than 50% of the data were
¹²⁸ contaminated in this way were masked as invalid.

¹²⁹ The second TTM deployment was ~~in 2014 from 06:00 on June from 0600 LT~~ 17 June 2014 to
¹³⁰ ~~05:00 on June 0500 LT~~ 19 (local time). June 2014. Two Nortek ADV-IMUs were mounted on this
¹³¹ TTM, with their heads spaced 0.5 m apart along the fin. In this case, the pressure cases and ADV
¹³² heads were inclined at an angle of 18° from normal to the leading edge of the fin to account for
¹³³ mooring blowdown during strong currents (Figure 3). This change was made to reduce vibrational
¹³⁴ motion observed during the June 2012 deployment that was believed to be associated with the
¹³⁵ orientation of the pressure cases. Their was no ADP on the anchor of this TTM.

¹³⁶ b. *The StableMoor platform*

¹³⁷ The second deployment platform was a cylindrical, StableMoorTM, syntactic foam buoy (man-
¹³⁸ ufacturer: Deep Water Buoyancy) that was anchored to a clump weight that weighed 1,200 kg
¹³⁹ (Figure 4). The buoy is 3.5 m long and 0.45 m in diameter with a tail ring that is 0.76 m in diame-
¹⁴⁰ ter. The StableMoor buoy (hereafter, ‘SMB’) weighs 295 kg in air, and has a buoyancy of 185 kg
¹⁴¹ in water.

¹⁴² The SMB was deployed with an ADV-IMU mounted at its nose from 11:21 on May 12 to 11:53
¹⁴³ on May 13, 2015 (local time). The sample volume of the ADV is 10 cm forward of the nose and 20
¹⁴⁴ cm above the center line of the SMB (Figure 4). Based on Wyngaard et al.’s (1985) investigation
¹⁴⁵ of a similarly shaped slender body, the velocity measurements should have flow-distortion effects
¹⁴⁶ of less than 10%. The SMB was equipped with a 1,200-kHz RDI workhorse sentinel ADP that
¹⁴⁷ was oriented downward-looking to measure water velocity below the platform in twelve 1-m bins
¹⁴⁸ and measure ~~bouy~~ platform motion (“bottom tracking”), all at a 1-Hz sample rate.

149 The SMB has two primary advantages compared to the TTM. First, it is significantly more
150 massive and hydrodynamically stable than the TTM, which reduces the frequency of motions of
151 the platform (Part I). Second, the SMB is capable of supporting a bottom-tracking ADP, which
152 provides an independent measure of the platform's translational motion. Disadvantages of the
153 SMB include: its size, which adds to the challenge of deployment and recovery, and its cost,
154 which is significantly higher than the TTM system.

155 *c. Turbulence Torpedo*

156 The turbulence torpedo is a simple sounding weight with an ADV head mounted forward of the
157 nose, and the ADV pressure case strapped below (Figure 5). This platform was deployed on May
158 14, 2015, for 37 minutes starting at 07:41 local time. This measurement was made from a davit
159 that hung the system from the side of the ship to a depth of approximately 25 m. The primary
160 advantages of this platform are its compact size, low cost, and the flexibility to perform spatial
161 transects.

162 *d. Coordinate system and turbulence averaging*

163 Unless stated otherwise, vector quantities in this work are in a fixed "principal-axes" coordinate
164 system that is aligned with the bidirectional tidal flow: positive u is in the direction of ebb (310°
165 True), positive w is vertically upward, and v is the cross-stream component in a right-handed
166 coordinate system (Figure 1). The full velocity vector, $\tilde{\mathbf{u}} = (\tilde{u}, \tilde{v}, \tilde{w})$, is separated into a mean and
167 turbulent component as $\tilde{\mathbf{u}} = \bar{\mathbf{u}} + \mathbf{u}$, where the over-bar denotes a 5-minute average. Turbulence
168 kinetic energy, $tke = \overline{u^2} + \overline{v^2} + \overline{w^2}$, and Reynold's stresses, \overline{uv} , \overline{uw} , \overline{vw} , are also estimated using
169 a 5-minute average. The horizontal velocity magnitude is computed as, $\bar{U} = (\bar{u}^2 + \bar{v}^2)^{1/2}$. The
170 friction velocity is estimated as, $u_* = (\overline{uw^2} + \overline{vw^2})^{1/4}$; note that this is taken at the height of the

¹⁷¹ ADV measurements, and should therefore only be interpreted as a proxy for the friction velocity
¹⁷² at the bottom boundary.

¹⁷³ All spectra, $S\{x\}(f) = |\mathcal{F}\{x(t)\}|^2$, and cross spectra, $C\{x,y\}(f) = \text{real}(\mathcal{F}\{x(t)\}\mathcal{F}\{y(t)\})$, are
¹⁷⁴ computed using NumPy fast Fourier transform routines (van der Walt et al. 2011). Here, $\mathcal{F}\{x(t)\}$
¹⁷⁵ denotes the fast Fourier transform of a signal $x(t)$ that has been linearly detrended and Hanning
¹⁷⁶ windowed to reduce spectral reddening.

¹⁷⁷ Throughout the remainder of this work, the dependence of S and C on f is im-
¹⁷⁸ plied (e.g., $S\{x\}(f)$ is hereafter $S\{x\}$), and for other variables the dependence on
¹⁷⁹ t is implied. Spectra and cross spectra are normalized to preserve variance; e.g.,
¹⁸⁰ $\int S\{u\} df = \bar{u^2}$, and $\int C\{u,v\} df = \bar{uv} \int S\{u\} df = \bar{u^2}$, and $\int C\{u,v\} df = \bar{uv}$. The notations
¹⁸¹ $S\{\mathbf{u}\} = (S\{u\}, S\{v\}, S\{w\})$, and $C\{\mathbf{u}\} = (C\{u,v\}, C\{u,w\}, C\{v,w\})$ denote the set of spectra and
¹⁸² cross spectra for each velocity component and pairs of components, respectively.

¹⁸³ Turbulence dissipation rates are computed as:

$$\varepsilon = \frac{1}{\bar{U}} \left(\alpha \left\langle (S\{u\} + S\{v\} + S\{w\}) f^{5/3} \right\rangle_{\text{fis}} \right)^{3/2} \quad (1)$$

¹⁸⁴ where $\alpha = 0.5$ and $\langle \rangle_{\text{fis}}$ denotes an average over the inertial subrange of the velocity spec-
¹⁸⁵ tra and where the signal-to-noise ratio is small (Lumley and Terray 1983; Sreenivasan 1995).
¹⁸⁶ Throughout this work, we take this average from 0.3 to 1 Hz for the u and v components, and 0.3
¹⁸⁷ to 3 Hz for the w component.

¹⁸⁸ 3. Methodology

¹⁸⁹ This work describes a method for correcting velocity measurements from a moving velocity
¹⁹⁰ sensor, $\tilde{\mathbf{u}}_m$, using independent measurements of that sensor's motion, $\tilde{\mathbf{u}}_h$, to remove the motion

191 from the velocity measurements, and thus estimate the ‘motion corrected velocity’:

$$\tilde{\mathbf{u}}(t) = \tilde{\mathbf{u}}_m(t) + \tilde{\mathbf{u}}_h(t) \quad . \quad (2)$$

192 Note here that the ‘+’-sign is correct because head motion, $\tilde{\mathbf{u}}_h$, induces a measured velocity in
 193 the opposite direction of the head motion itself ($\tilde{\mathbf{u}}_m = \tilde{\mathbf{u}} - \tilde{\mathbf{u}}_h$). This approach has been used
 194 to successfully correct sonic anemometer measurements of atmospheric turbulence (e.g., Edson
 195 et al. 1998; Miller et al. 2008). In the ocean, previous works have utilized inertial motion sensors
 196 to quantify the motion of multiscale profilers for the purpose of measuring the full spectrum of
 197 oceanic shear (Winkel et al. 1996), and to quantify the motion of thermistor sensors (Moum and
 198 Nash 2009), but the Edson et al. (1998) approach has not been documented for moored ADV
 199 measurements.

200 The Microstrain IMU available in the Nortek Vector ADV measures the linear acceleration,
 201 $\mathbf{a}^*(t)$, rotational motion, $\boldsymbol{\omega}^*(t)$, and orientation matrix in the earth’s reference frame, $\mathbf{R}(t)$,
 202 \mathbf{R} , of the ADV pressure case in the Earth reference frame at every time step of the ADV’s sam-
 203 pling. The ‘*’ superscripts denote that these vectors are measured in the ADV’s local coordinate
 204 system. They can be rotated into the earth frame using the inverse of the orientation matrix, e.g.,
 205 $\mathbf{a}(t) = \mathbf{R}^T(t) \cdot \mathbf{a}^*(t)$. The motion of the ADV head is calculated from these signals as the sum of
 206 rotational and translational motion:

$$\begin{aligned} \tilde{\mathbf{u}}_h &= \tilde{\mathbf{u}}_\omega + \tilde{\mathbf{u}}_\mathbf{a} + \tilde{\mathbf{u}}_{\text{low}} \\ &= \mathbf{R}^T(t) \cdot (\boldsymbol{\omega}^*(t) \times \ell^*) + \int \langle \mathbf{a}(t) \rangle_{f_a} dt + \tilde{\mathbf{u}}_{\text{low}}(t) \end{aligned} \quad (3)$$

207 Here ‘*’ superscripts denote quantities in the ADV’s local coordinate system, and ℓ^* is the vector
 208 from the IMU to the ADV head. \mathbf{R}^T —the inverse of the orientation matrix—rotates vectors from
 209 the ADV to the Earth reference frame. The , and the notation $\langle \cdot \rangle_{f_a}$ indicates a high-pass filtering
 210 operation at frequency f_a . The high-pass filter reduces low-frequency noise in \mathbf{a} —sometimes

referred to as bias drift—that is amplified by integration (Barshan and Durrant-Whyte 1995; Bevly 2004; Gulmammadov 2009). $\tilde{\mathbf{u}}_{\text{low}}$ is the low-frequency translational motion that is unresolved by $\tilde{\mathbf{u}}_{\mathbf{a}}$, and it is discussed in more detail below. To avoid double counting, $\tilde{\mathbf{u}}_{\text{low}}$ should be estimated by applying the complementary low-pass filter (i.e., at f_a) to the independent measurement of low-frequency motion. We use fourth order, zero-phase (bidirectional), Hanning filters for all filtering operations.

The noise levels of the IMU, \mathbf{n}_{ω} and \mathbf{n}_a , are computed from ADV-IMU data collected while the instrument was resting motionless on a table for several hours. Where, for this motionless dataset, the noise levels are defined according to (3) with \mathbf{n}_{ω} in place of $\tilde{\mathbf{u}}_{\omega}$, and \mathbf{n}_a in place of $\tilde{\mathbf{u}}_a$.

For quantifying \mathbf{n}_{ω} we assume that $|\ell^*| = 1$, which is the approximate length of the ADV head cable. $S\{\mathbf{n}_{\omega}\}$ is equal in all three components, because the rotation-rate sensor noise-levels are independent of orientation (Figure 6, yellow). $S\{\mathbf{n}_{\omega}\}$ is several orders of magnitude lower than the velocity spectra we measured (grey region), and also more than an order of magnitude smaller than the Doppler noise levels of the ADV. ~~Here we have used $\ell^* = 1 \text{ m}$; which is the order-of-magnitude of the typical distance between the ADV head and the IMU.~~ This indicates that the precision of $\tilde{\mathbf{u}}_{\omega}$ (i.e. the angular rate sensor) is adequate for making corrections to ADV velocity measurements.

The noise level of $S\{\tilde{\mathbf{u}}_a\}$ (Figure 6, black), on the other hand, is dominated by a f^{-2} slope that results from integrating the low-frequency noise in \mathbf{a} . The horizontal (u and v) spectra of these noise levels are identical, and so we only present one of them for simplicity (solid lines). The vertical spectra noise levels are different because the signal-to-noise ratio is larger (dashed black lines). High-pass filtering reduces the low-frequency noise (blue and red) so that it does not contaminate motion correction, but any real motion that does exist at these frequencies is lost (Egeland 2014; VanZwieten et al. 2015). This means there is a residual low-frequency translational

234 motion, $\tilde{\mathbf{u}}_{\text{low}}$, that needs to be measured independently—or at the very least considered—when
235 using ADV-IMU data from moving platforms.

236 For the SMB, the ADP bottom-track measured $\tilde{\mathbf{u}}_{\text{low}}$, and this measurement agrees with $\tilde{\mathbf{u}}_{\mathbf{a}}$ over
237 a narrow frequency band (see Part I, appendix A), indicating that the ADP and IMU are resolving
238 the same motion. When this is the case, it is trivial to select a frequency in the middle of the
239 spectral overlap (in this case, we choose $f_a = 0.2$ Hz), and high-pass and low-pass filter $\tilde{\mathbf{u}}_{\mathbf{a}}$ and
240 $\tilde{\mathbf{u}}_{\text{low}}$, respectively, then sum to estimate total translational motion.

241 The position of the TTM ADV can be estimated, relative to its baseanchor, by assuming the
242 mooring acts like a rigid pole and using the IMU orientation matrix to estimate the pole’s ‘lean’.
243 The position obtained from this model can then be differentiated to estimate $\tilde{\mathbf{u}}_{\text{low}}$ (this model does
244 not apply at high frequencies). Spectra of $\tilde{\mathbf{u}}_{\text{low}}$ estimated using this approach for the June 2014
245 TTM deployment (Figure 6, bluegreen) are plotted up to the point where they cross their respec-
246 tive $S\{\tilde{\mathbf{u}}_{\mathbf{a}}\}$ noise level (black). Together, these two lines provide an ‘aggregate noise level’ of
247 translational velocity estimates for the TTM: the rigid pole estimate of $\tilde{\mathbf{u}}_{\text{low}}$ indicates the ampli-
248 tude of unresolved motion at low- f (green), and $S\{\tilde{\mathbf{u}}_{\mathbf{a}}\}$ indicates the limits of the IMU at high- f
249 (blueblack). Coincidentally, $S\{\langle \tilde{\mathbf{u}}_{\mathbf{a}} \rangle_{0.03\text{Hz}}\}$ is not a terrible approximation for this aggregate noise
250 level. Furthermore, because this aggregate noise level is ~~more than an order of magnitude lower~~
251 at least a factor of 4 smaller than the velocity spectra ~~of interest we measured~~ (shaded region), the
252 results of motion correction are ~~essentially identical not sensitive to~~ whether we use the rigid pole
253 model to estimate $\tilde{\mathbf{u}}_{\text{low}}$, or if we simply assume that $\tilde{\mathbf{u}}_{\text{low}} = 0$.

254 The choice of f_a does influence the effectiveness of motion correction (Figure 7). When f_a is too
255 high (e.g., 0.3 Hz, red), the high-pass filter removes resolved motion from $\tilde{\mathbf{u}}_h$ that could be used
256 to correct velocity measurements. In particular, notice that the amplitude of the 0.15 Hz peak—
257 which is clearly the result of motion contamination (grey line)—is reduced significantly when we

258 preserve more $\tilde{\mathbf{u}}_h$ information by reducing the high pass filter frequency to $f_a = 0.03$ Hz. Further
259 reducing f_a to 0.003 Hz does not reduce the peak further, but does increase the amplitude of
260 the spectra at low-frequency. This ~~low- f~~ increase is the IMU-accelerometer's low-frequency bias
261 drift (Figure 6) ~~returning to contaminate the motion correction method~~contaminating the velocity
262 measurements. Therefore, we conclude that $f_a = 0.03$ Hz is a convenient ‘middle’ frequency
263 that reduces accelerometer bias-drift without destroying resolved motion of the TTM. The same
264 $f_a = 0.03$ Hz filter was selected, based on a similar analysis, for the turbulence torpedo.

265 Thus, we find that filter selection involves a trade-off between filtering out the bias drift noise
266 at low-frequencies while not filtering out measured motion at high frequencies. In general, this
267 will depend on the dynamics of the platform used to support the ADV, and the intensity of the
268 turbulence being measured. When an independent measurement of $\tilde{\mathbf{u}}_{\text{low}}$ is available the cross-
269 coherence with $\tilde{\mathbf{u}}_a$ can indicate a region of spectral overlap, and f_a can be selected at the midpoint.
270 Lacking a reliable estimate of $\tilde{\mathbf{u}}_{\text{low}}$, the value of f_a that produces the lowest tke estimates is likely
271 the best.

272 Additional details on motion correction—including a detailed accounting of the distinct co-
273 ordinate systems of the IMU, ADV pressure case, and ADV head—can be found in Kilcher
274 et al. (2016). Open-source Python tools for performing motion correction of ADV-IMU data—
275 including scripts that write processed data in Matlab and tabulated formats—are available at
276 <http://lkilcher.github.io/dolfin/>.

277 **4. Results**

278 *a. Mean velocity*

279 Figure 8 shows a comparison of $\bar{\mathbf{u}}$ measured by an ADV-IMU mounted on the TTM, to an
280 upward-looking ADP on the anchor. The profiler measurements—taken at the same depth as the
281 ADV on the TTM—were contaminated by acoustic reflection from the strongback fin when it
282 was inline with one of the profiler’s beams –(see section 2.a.). When those points (not shown in
283 the figure) are excluded, this comparison shows excellent agreement between the ADV and ADP
284 measurements of mean velocity. The \bar{u} , \bar{v} , and \bar{w} components have a root-mean-square error of
285 0.05, 0.13, and 0.03 m/sms⁻¹, respectively. Although it is important to note that there is some
286 discrepancy between ADP- and ADV-measured velocities (especially in \bar{v} , which is most likely
287 due to incomplete motion correction), the agreement between the magnitude and direction of these
288 independent velocity measurements indicates that moored ADV-IMUs provide a reliable estimate
289 of mean velocity in the Earth’s reference frame.

290 *b. TTM spectra*

291 As discussed in detail in Part 1, the mooring motion of the TTM, $S\{\mathbf{u}_h\}$, has a peak at 0.1 to 0.2
292 Hz from swaying of the mooring that is most likely driven by eddy shedding from the spherical
293 buoy (Figure 9, red lines). There is also higher-frequency broadband motion that is associated with
294 fluttering of the strongback fin around the mooring line. These motions are especially energetic
295 in $S\{v\}$ because this is the direction in which the TTM is most unstable. As is expected from
296 fluid-structure interaction theory, the amplitude of these motions increases with increasing mean
297 velocity (Morison et al. 1950).

298 The mooring motion contaminates the uncorrected ADV measurements of velocity, $S\{\mathbf{u}_m\}$,
299 whenever the amplitude of the motion is similar to or greater than the amplitude of the turbulence.
300 Fortunately, much of this motion can be removed as detailed in Section 3. At high frequencies
301 ($f > 0.3$ Hz) for each mean-flow speed ~~the measurements~~ $S\{\mathbf{u}\}$ are consistent with Kolmogorov's
302 (1941) theory of isotropic turbulence: the spectra decay with a $f^{-5/3}$ slope and have equal ampli-
303 tude across the velocity components. At lower frequencies, the spectral 'roll-off' shape is similar
304 to that measured by several others (e.g., Thomson et al. 2012; McMillan et al. 2016). The degree
305 of agreement between Kaimal et al.'s (1972) semi-empirical form (cyan) and $S\{\mathbf{u}\}$ is similar to
306 that of Walter et al. (2011). This suggests that bottom-boundary layer physics are contributing to
307 the turbulence at this site and depth.

308 For $|\mathbf{u}| > 1.0 \text{ ms}^{-1}$, motion correction improves $S\{u\}$ and $S\{v\}$ at frequencies as high as 3
309 Hz. This indicates that tight synchronization between the ADV and IMU is important and that
310 implementing asynchronous approaches to motion correction may be challenging.

311 As successful as motion correction is, some motion contamination is 'persistent'. This is most
312 notable in $S\{v\}$ at the highest flow speeds ($> 2.0 \text{ m/s}$): a peak at 0.15 Hz is an order of mag-
313 nitude larger than a smooth spectral shape would suggest. This persistent motion contamination
314 is evident to a lesser degree in $S\{u\}$ for $|u| > 2 \text{ m/s}$, and in $S\{v\}$ at lower flow speeds. $S\{w\}$
315 appears to have no persistent motion contamination because the amplitude of the motion in this
316 direction is much lower than the measured spectra.

317 The amplitude of the persistent motion contamination peaks in $S\{v\}$ at 0.15 Hz is a factor of 5 to
318 10 times smaller than the amplitude of the ADV head motion itself. This observation suggests that
319 the Microstrain IMU can be used to effectively correct mooring motion at this frequency when the
320 amplitude of that motion is less than 5 times the amplitude of the real turbulence spectrum. As a
321 result, we have chosen a value of 3 as a conservative estimate of motion correction's effectiveness.

322 In addition to the primary benefit of correcting for mooring motion, the IMU measurements
323 can also be used to identify and screen out persistent motion contamination. For example, one
324 of the most common uses of turbulence spectra is for the calculation of ϵ and tke. For these
325 purposes, and based on the relative amplitudes of the 0.15-Hz peaks, we assume that persistent
326 motion contamination is likely where $S\{\mathbf{u}_h\}/S\{\mathbf{u}\} > 3$, and thereby exclude these regions from
327 spectral fits.

328 In the present case, for u - and w -component spectra, this criteria only excludes a narrow range of
329 frequencies at the 0.15-Hz motion peak [for the largest flow speeds](#). This criteria is more restrictive
330 of v -component spectra at high frequencies for $\bar{U} > 1.0 \text{ ms}^{-1}$, but this may be acceptable because
331 the amplitude of $S\{v\}$ at these frequencies—i.e., in the isotropic inertial subrange—should be
332 equal to that of $S\{u\}$ and $S\{w\}$ (Kolmogorov 1941).

333 Agreement of $S\{v\}$ with that of $S\{u\}$ and $S\{w\}$ at frequencies $> 0.3 \text{ Hz}$ indicates that motion
334 correction is effective at those frequencies even when $S\{\mathbf{u}_h\}/S\{\mathbf{u}\} \gtrsim 3$. This outcome suggests
335 that our screening threshold is excessively conservative at those frequencies, and that a more pre-
336 cise screening threshold may be frequency dependent. For example, it might take into account the
337 f^{-2} character of the noise in $S\{\mathbf{u}_a\}$ (Figure 6). For the purpose of this work, the $S\{\mathbf{u}_h\}/S\{\mathbf{u}\} < 3$
338 threshold for spectral fits is sufficient, and detailed characterization of the IMU’s motion- and
339 frequency-dependent noise level is left for future work.

340 *c. StableMoor Spectra*

341 Spectra of SMB motion have broader peaks, with a maximum amplitude that is approximately
342 half the frequency of the TTM spectral peak (0.06 Hz, Figure 10). The motion of this platform
343 also does not have high-frequency “subpeaks” or other high-frequency broadband excitation (Part

344 1). These characteristics ~~of the motion are most likely are~~ due to the more massive and hydrodynamically streamlined properties of the SMB compared to the TTM.

346 Like the TTM, the motion-corrected spectra from the SMB are consistent with turbulence theory
347 and previous observations. A notable distinction from the TTM, however, is that there are no
348 obvious persistent motion contamination peaks. That is, this measurement system provides an
349 accurate estimate of the turbulence spectra at this location from low frequencies to more than 1
350 Hz—well into the inertial subrange—for all three components of velocity.

351 Note that this level of accuracy cannot be obtained without the independent estimate of \mathbf{u}_{low}
352 (from the bottom-tracking ADP). If we assume that $\mathbf{u}_{\text{low}} = 0$, a similar plot to Figure 10 (not
353 shown) reveals persistent motion-contamination peaks and troughs in $S\{u\}$ and $S\{v\}$ regardless
354 of the choice of f_a . This indicates that the low-frequency translational motion of the SMB that
355 is important to motion correction is poorly resolved by the IMU’s accelerometer. In other words,
356 compared to the TTM, the SMB provides a more accurate measurement of turbulence when it
357 includes an independent measure of \mathbf{u}_{low} , but it does no better—and perhaps worse—when it does
358 not.

359 *d. Torpedo spectra*

360 $S\{u_h\}$ and $S\{v_h\}$ for the turbulence torpedo is broadband and $S\{w_h\}$ motion has a narrow peak
361 at 0.3 Hz (Figure 11). Because \mathbf{u}_h is estimated using $f_a = 0.03$ Hz and assuming $\mathbf{u}_{\text{low}} = 0$, its
362 spectra rolls off quickly below f_a . Motion correction of the torpedo data appears to effectively
363 remove a motion peak from $S\{w\}$ at 0.3 Hz, and corrects $S\{v\}$ between 0.04 and 0.6 Hz. $S\{u\}$
364 is mostly unaffected by motion at these frequencies, because the torpedo motion is smaller than
365 the turbulence in this direction. At frequencies below f_a , $S\{u\}$ and $S\{v\}$ increase dramatically.
366 This suggests that unresolved, low-frequency motion of the torpedo is contaminating the velocity

367 measurements at these frequencies. It may be possible to correct for some of this contamination
368 using a measurement of the ship's motion as a proxy for the torpedo's low-frequency motion,
369 but this has not been done. Still, above f_a , the torpedo appears to provide a reliable estimate of
370 spectral amplitude in the inertial subrange and can therefore be used to estimate ε . Considering
371 the simplicity of the platform, it may be a useful option for quantifying this turbulence statistic in
372 a variety of scenarios. If a GPS is positioned above it, it may be capable of providing even more.

373 *e. Cross Spectra*

374 Cross-spectra indicate the correlation between different velocity components as a function of fre-
375 quency, and their integrals are the Reynold's stresses. Head motion cross-spectra, $C\{\mathbf{u}_h\}$ (Figure
376 12, red), and uncorrected velocity cross-spectra, $C\{\mathbf{u}_m\}$ (black), from TTM measurements have
377 large peaks at the same frequency (0.15 Hz) as peaks in auto-spectra (Figure 9). This indicates
378 that mooring motion contaminates the uncorrected cross-spectral velocity measurements, and that
379 Reynold's stress estimates based on uncorrected velocity measurements will be contaminated by
380 mooring motion.

381 Fortunately, motion corrected velocity cross-spectra, $C\{\mathbf{u}\}$ ([Figure 12](#), blue), have reduced
382 cross-spectral amplitudes at these frequencies. This indicates that motion correction reduces mo-
383 tion contamination to produce more reliable estimates of velocity cross spectra and Reynold's
384 stresses (Figure 12). Notably, the low standard deviation of $f \cdot C\{\mathbf{u}\} - f C\{\mathbf{u}\}$ (indicated by the
385 blue shading) compared to the mean values of $C\{\mathbf{u}_h\}$ and $C\{\mathbf{u}_m\}$ —at the
386 frequencies of maximum motion—indicates that even the individual values of $C\{\mathbf{u}\}$ are reduced
387 at these frequencies, compared to $C\{\mathbf{u}_m\}$, not just their mean.

388 These results indicate that motion-corrected TTM velocity measurements can be used to estimate
389 turbulence Reynold's stresses. Without motion correction, Reynold's stress estimates would be

390 contaminated by the large peaks in the cross spectra that are caused by the swaying and fluttering
391 motion of the TTM vane. Cross-spectra of TTM data for other velocity ranges (i.e., $< 2 \text{ ms}^{-1}$),
392 and cross-spectra from the SMB show similar results (not shown). However, we note that because
393 the SMB is less-stable in pitch than the TTM (see Part I for details), the TTM provides a more
394 accurate estimates of \bar{uw} .

395 In order to compare the cross-spectra to other measurements, we normalize them follow-
396 ing Kaimal et al. (1972) as: $\hat{C}\{u,w\}(\hat{f}) = -C\{u,w\}f_*/u_*^2 \hat{C}\{u,w\}(\hat{f}) = -C\{u,w\}f_* / u_*^2$, where
397 $f_* = \bar{U}/z$ and $\hat{f} = f/f_*$. When plotted on a log-log scale, $\hat{C}\{u,w\}$ has a $\hat{f}^{-7/3}$ high-frequency
398 spectral slope that is consistent with other measurements (Figure 13). At low-frequency, the cross-
399 spectra are more than 10x smaller than the semi-empirical Kaimal form, but this discrepancy is
400 consistent with other measurements of cross-spectra. In particular, Walter et al. (2011) observed
401 a half-decade reduction from the Kaimal form near the seafloor, and measurements from an ADV
402 positioned 4.6 m above the seafloor on a fixed tripod at a different site in Puget Sound show a
403 similar degree of deviation as observed here (Thomson et al. 2012).

404 While one might be inclined to attribute the discrepancy between these estimates and the Kaimal
405 form to normalization by local u_* , the agreement between auto-spectra and their Kaimal form
406 suggests otherwise (Figure 9). Instead, we conclude that either the Kaimal cross-spectra do not
407 apply universally at distances far from the bottom boundary, or the spectra are being modified
408 by physics other than bottom boundary layer driven turbulence. Either way, the agreement of
409 TTM-measured cross-spectra with measurements from stationary platforms is interpreted as an
410 encouraging sign indication that this platform can resolve cross-spectra and Reynold's stresses.

411 **5. Discussion**

412 Ideally, moored motion-corrected turbulence velocity measurements would be validated against
413 simultaneous independent validated measurements of turbulence velocity at the same scales, time,
414 and location. Accomplishing this, however, involves significant technical challenges that are not
415 easily overcome—most notably the difficulty of measuring turbulence at the same point as the
416 moving ADV. A slightly less ideal but much more realistic confirmation of the methodology might
417 involve comparing the statistics of moored turbulence measurements to those from a nearby fixed
418 platform, or a fixed platform placed at the same location at a different time (e.g., the “tripod”
419 platform described in Thomson et al. 2012). Unfortunately, to our knowledge, these measurements
420 have not yet been made.

421 The previous section showed that the shape of the turbulence velocity spectra from moored
422 ADVs is consistent with Kolmogorov’s theory of locally isotropic turbulence, which has been ob-
423 served consistently in turbulence measurements for decades (Kolmogorov 1941; Grant et al. 1962;
424 McMillan et al. 2016). This is interpreted as the first indication that the measurement systems
425 presented are capable of accurately resolving turbulence. The degree to which uncorrected spec-
426 tra were corrected toward this theoretical and observationally confirmed shape is interpreted as a
427 measure of the improvement of the spectral estimates by motion correction. This section takes
428 that reasoning one step further to demonstrate that motion-corrected velocity measurements can
429 produce estimates of turbulence statistics that are consistent with the physical processes that can
430 be reasonably assumed to dominate the measurement site.

431 Figure 14 presents a time series of the mean velocity (A) and several turbulence statistics that
432 were measured during the June 2014 TTM deployment. This figure shows the evolution of the flow
433 through Admiralty Inlet during 1.5 tidal cycles. The tke (B), Reynold’s stresses (C), dissipation,

⁴³⁴ and one component of turbulence production (D) grow and strengthen with ebb or flood then
⁴³⁵ subside during slack tide. This component of turbulence production is:

$$P_{uz} = \overline{uw} \frac{\partial \bar{u}}{\partial z} . \quad (4)$$

⁴³⁶ Where $\partial \bar{u} / \partial z$ is computed from the two ADVs on the TTM. The highest values of ε and P_{uz} occur
⁴³⁷ at the peak of the ebb or flood, which is in agreement with other measurements in tidal channels.
⁴³⁸ The agreement of the magnitude of P_{uz} with ε at those times suggests a local production-dissipation
⁴³⁹ balance that is often observed in tidally forced channels (Trowbridge et al. 1999; Stacey et al.
⁴⁴⁰ 1999b; McMillan et al. 2016). At other times, the value of P_{uz} is insufficient to balance ε or is
⁴⁴¹ negative.

⁴⁴² Inspection of the negative P_{uz} values reveals that most of them are caused by a reversed sign of \overline{uw}
⁴⁴³ rather than a reversed sign of $\partial u / \partial z$ (i.e., when compared to the sign of u). This finding suggests
⁴⁴⁴ that uncertainty in \overline{uw} may be contributing to discrepancies between P_{uz} and ε . Furthermore,
⁴⁴⁵ considering the complex nature of the bathymetry and shoreline at this site (i.e., the headland), it
⁴⁴⁶ is not surprising that P_{uz} does not perfectly balance ε . Other terms of the tke equation are likely
⁴⁴⁷ to be important, such as turbulence advection, other components of production, and turbulent
⁴⁴⁸ transport. The fact that P_{uz} and ε are in near balance as often as they are indicates that bottom
⁴⁴⁹ boundary layer physics are important to the turbulence dynamics at this site.

⁴⁵⁰ Given the assumptions implicit in this comparison and the discussion above, agreement between
⁴⁵¹ P_{uz} and ε —especially for the highest values of ε —suggests the turbulent boundary layer reaches
⁴⁵² the depth of these measurements (10 m) during the highest flow speeds (Figure 15). This result
⁴⁵³ is further supported by a comparison of \bar{U} with ε (Figure 16). Here we see a $\varepsilon \propto \bar{U}^3$ dependence
⁴⁵⁴ that is again suggestive of bottom boundary layer physics (Trowbridge 1992; Nash et al. 2009). At

455 lower flow speeds, ε deviates from this relationship, which suggests that the boundary layer is no
456 longer the dominant physical process at the depth of these measurements.

457 There are two intriguing differences between the ebb and flood datasets: 1) the drag coefficient
458 relating ε to \bar{U}^3 is larger for ebbs, and 2) the fit does not hold as well for low flow speeds (Figure
459 16). These details are not surprising considering the complex bathymetry at the test site (Figure
460 1). In particular, the flow immediately upstream of the measurement site is exposed to much
461 more bathymetric curvature—i.e. from the headland—during ebb (when \bar{u} is > 0) than during
462 flood ($\bar{u} < 0$). Based on this, one might expect flow separation (turbulence advection), turbulence
463 production, or turbulence transport emanating from the headland to have a stronger impact on
464 the flow at this site during ebb than flood. These effects are a likely contributor to the distinct
465 relationships observed in Figure 16.

466 The hypothesis that the headland is a key contributor to the turbulence dynamics at this site
467 suggests that terms such as cross-stream turbulence advection, $\bar{v}\partial tke/\partial y$, the lateral turbulent
468 transport terms, $\partial\bar{u}_i\bar{u}_i\bar{v}/\partial y$, or lateral shear production, $\bar{u}\bar{v}\partial\bar{u}/\partial y$, may contribute significantly to
469 the dynamics of turbulence at this site. While we did not measure stratification profiles during
470 these measurements, we do not typically expect buoyancy flux to play [a](#) dominant role due to the
471 fact that this region tends to be tidally well-mixed (Geyer and Cannon 1982). In summary, bottom
472 boundary layer physics seems to be the dominant process at the measurement site, with lateral
473 advection, lateral transport, and lateral production of tke also potentially contributing—especially
474 during ebb. A more detailed analysis of the turbulence and momentum dynamics of this headland
475 is left for future work (e.g., [Warner et al. 2013](#))[\(e.g., similar to Warner et al. 2013\)](#).

476 **6. Conclusion**

477 This work presents a methodology for measuring turbulence from moored ADV-IMUs and
478 demonstrates that motion correction reduces mooring motion-contamination. Comparison of spec-
479 tra of ADV head motion, $S\{\mathbf{u}_h\}$, to that of motion-corrected, $S\{\mathbf{u}\}$, and uncorrected spectra,
480 $S\{\mathbf{u}_m\}$, reveals that motion correction improves spectral estimates of moored ADV measurements.
481 In particular, we found that motion-corrected spectra have spectral shapes that are similar to previ-
482 ous measurements of tidal-channel turbulence and have $f^{-5/3}$ spectral slopes at high frequencies.
483 This finding suggests that the motion-corrected spectra resolve the inertial subrange predicted by
484 Kolmogorov's theory of locally isotropic turbulence.

485 Motion correction reduces motion contamination for all platforms we presented but it does not
486 necessarily remove it completely. This outcome seems to depend on the relative amplitude of plat-
487 form motion compared to the underlying turbulence being measured. The most notable example
488 of this is from TTM $S\{v\}$, which have large-amplitude “swaying” peaks at 0.15 Hz that interrupts
489 the frequently observed ‘roll-off’ between the low-frequency ‘energy containing scales’ and the
490 $f^{-5/3}$ inertial subrange.

491 The possibility of persistent motion contamination requires that turbulence measurements from
492 moored, motion-corrected ADV-IMUs be interpreted with care. An inspection of spectra presented
493 here suggests that excluding spectral regions where $S\{\mathbf{u}_h\}/S\{\mathbf{u}\} > 3$ removes persistent-motion
494 contamination peaks while still preserving spectral regions where motion correction is effective.
495 Using this criteria, it is then possible to produce spectral fits that exclude persistent-motion con-
496 tamination, and provide reliable estimates of turbulence quantities of interest (e.g., ε and tke).

497 We have also shown that motion correction reduces motion contamination in cross spectra. This
498 finding is important because it suggests that moored ADV-IMU measurements may be used to

499 produce reliable estimates of Reynolds stresses. We utilized these stress estimates and vertical
500 shear estimates, both from the TTM, to estimate P_{uz} .

501 Finally, we have shown that ε estimates based on motion-corrected spectra scale with \bar{U}^3 , and
502 balance P_{uz} estimates during peak ebb and flood. Together, these results indicate that bottom
503 boundary layer physics are a dominant process at this site, and that the boundary layer reaches the
504 height of the ADV-IMUs (10 m) during ebb and flood. The degree of agreement between P_{uz} and ε
505 also serves as an indicator of the self-consistency of moored ADV-IMU turbulence measurements.

506 *Acknowledgments.* Many thanks to Joe Talbert, Alex DeKlerk, Captain Andy Reay-Ellers, Jen-
507 nifer Rinker, Maricarmen Guerra, and Eric Nelson in assisting with data collection. The authors
508 are also grateful to James VanZwieten, Matthew Egeland and Marshall Richmond for discussion
509 on the details of this work.

510 Thanks to the open-source software community for the tools used in this work, especially the
511 developers of L^AT_EX, Python, NumPy, Matplotlib, git, and GNU emacs.

512 This work was supported by the U.S. Department of Energy under Contract No. DE-AC36-
513 08GO28308 with the National Renewable Energy Laboratory. Funding for the work was provided
514 by the DOE Office of Energy Efficiency and Renewable Energy, Wind and Water Power Technolo-
515 gies Office.

516 The U.S. Government retains and the publisher, by accepting the article for publication, ac-
517 knowledges that the U.S. Government retains a nonexclusive, paid-up, irrevocable, worldwide
518 license to publish or reproduce the published form of this work, or allow others to do so, for U.S.
519 Government purposes.

520 **References**

- 521 Afgan, I., J. McNaughton, S. Rolfo, D. Apsley, T. Stallard, and P. Stansby, 2013: Turbulent flow
522 and loading on a tidal stream turbine by les and rans. *International Journal of Heat and Fluid*
523 *Flow*, **43**, 96–108.
- 524 Alexander, S. R., and P. E. Hamlington, 2015: Analysis of turbulent bending moments in tidal
525 current boundary layers. *Journal of Renewable and Sustainable Energy*, **7 (6)**, 063 118.
- 526 Alford, M. H., 2010: Sustained, full-water-column observations of internal waves and mixing near
527 mendocino escarpment. *Journal of Physical Oceanography*, **40 (12)**, 2643–2660, doi:10.1175/
528 2010JPO4502.1.
- 529 Axford, D., 1968: On the accuracy of wind measurements using an inertial platform in an aircraft,
530 and an example of a measurement of the vertical mesostructure of the atmosphere. *Journal of*
531 *Applied Meteorology*, **7 (4)**, 645–666.
- 532 Barshan, B., and H. F. Durrant-Whyte, 1995: Inertial navigation systems for mobile robots. *IEEE*
533 *Transactions on Robotics and Automation*, **11 (3)**, 328–342.
- 534 Bevly, D. M., 2004: Global positioning system (gps): A low-cost velocity sensor for correcting in-
535 erial sensor errors on ground vehicles. *Journal of dynamic systems, measurement, and control*,
536 **126 (2)**, 255–264.
- 537 Cartwright, G. M., C. T. Friedrichs, P. J. Dickhudt, T. Gass, and F. H. Farmer, 2009: Using the
538 acoustic doppler velocimeter (adv) in the mudbed real-time observing system. *Marine Technol-
539 ogy for Our Future: Global and Local Challenges*.
- 540 Doherty, K., D. Frye, S. Liberatore, and J. Toole, 1999: A moored profiling instrument*. *Journal*
541 *of Atmospheric and Oceanic Technology*, **16 (11)**, 1816–1829.

- 542 Edson, J. B., A. A. Hinton, K. E. Prada, J. E. Hare, and C. W. Fairall, 1998: Direct covariance
543 flux estimates from mobile platforms at sea*. *Journal of Atmospheric and Oceanic Technology*,
544 **15** (2), 547–562, doi:10.1175/1520-0426(1998)015<0547:DCFEFM>2.0.CO;2.
- 545 Egeland, M. N., 2014: Spectral evaluation of motion compensated ADV systems for ocean turbu-
546 lence measurements. Ph.D. thesis, Florida Atlantic University.
- 547 Fer, I., and M. B. Paskyabi, 2014: Autonomous ocean turbulence measurements using shear probes
548 on a moored instrument. *Journal of Atmospheric and Oceanic Technology*, **31** (2), 474–490, doi:
549 10.1175/JTECH-D-13-00096.1.
- 550 Finlayson, D., 2005: Combined bathymetry and topography of the Puget Lowlands,
551 Washington state. URL <https://www.ocean.washington.edu/data/pugetsound/psdem2005.html>,
552 g1230485.zip, retrieved September 2014.
- 553 Geyer, R. W., M. E. Scully, and D. K. Ralston, 2008: Quantifying vertical mixing in estuaries.
554 *Environmental Fluid Mechanics*, **8**, 495–509, doi:10.1007/s10652-008-9107-2.
- 555 Geyer, W. R., and G. A. Cannon, 1982: Sill processes related to deep water renewal in a fjord. *Jour-*
556 *nal of Geophysical Research: Oceans*, **87** (C10), 7985–7996, doi:10.1029/JC087iC10p07985.
- 557 Goodman, L., E. R. Levine, and R. G. Lueck, 2006: On measuring the terms of the turbulent
558 kinetic energy budget from an auv. *Journal of Atmospheric and Oceanic Technology*, **23** (7),
559 977–990, doi:10.1175/JTECH1889.1.
- 560 Grant, H. L., R. W. Stewart, and A. Moilliet, 1962: Turbulence spectra from a tidal channel.
561 *Journal of Fluid Mechanics*, **12**, 241–263.
- 562 Guerra Paris, M., and J. Thomson, 2017: Turbulence measurements from 5-beam acoustic doppler
563 current profilers. *Journal of Atmospheric and Oceanic Technology*.

- 564 Gulmammadov, F., 2009: Analysis, modeling and compensation of bias drift in mems inertial
565 sensors. *Recent Advances in Space Technologies, 2009. RAST'09. 4th International Conference*
566 on, IEEE, 591–596.
- 567 Gunawan, B., V. S. Neary, and J. Colby, 2014: Tidal energy site resource assessment in the East
568 River tidal strait, near Roosevelt Island, New York, NY (USA). *Renewable Energy*, **71**, 509–
569 517, doi:10.1016/j.renene.2014.06.002.
- 570 Hand, M. M., N. D. Kelley, and M. J. Balas, 2003: Identification of wind turbine response to
571 turbulent inflow structures. Tech. Rep. NREL/CP-500-33465, National Renewable Energy Lab-
572 oratory.
- 573 Harding, S., L. Kilcher, and J. Thomson, 2017: Turbulence measurements from compliant moor-
574 ings - part 1: Motion characterization, in review.
- 575 Kaimal, J. C., J. C. Wyngaard, Y. Izumi, and O. R. Cote, 1972: Spectral characteristics of surface-
576 layer turbulence. *Quart. J. Roy. Meteor. Soc*, **98 (417)**, 563–689.
- 577 Kelley, N. D., B. J. Jonkman, G. N. Scott, J. T. Bialasiewicz, and L. S. Redmond, 2005: The impact
578 of coherent turbulence on wind turbine aeroelastic response and its simulation. *WindPower*,
579 Denver, Colorado, NREL/CP-500-38074, may 15-18.
- 580 Kilcher, L., J. Thomson, and S. Harding, 2017: Admiralty inlet advanced turbulence measure-
581 ments: final data and code archive [data set]. URL <http://mhkdir.openei.org/submissions/223>,
582 created 05-31-2017.
- 583 Kilcher, L., J. Thomson, J. Talbert, and A. DeKlerk, 2016: Measuring turbulence from moored
584 acoustic Doppler velocimeters: A manual to quantifying inflow at tidal energy sites. 9 62979,
585 National Renewable Energy Laboratory. URL www.nrel.gov/docs/fy16osti/62979.pdf.

- 586 Kim, S. C., C. T. Friedrichs, J. P.-Y. Maa, and L. D. Wright, 2000: Estimating bottom stress in
587 tidal boundary layer from acoustic doppler velocimeter data. *Journal of Hydraulic Engineering*,
588 399–406.
- 589 Kolmogorov, A. N., 1941: Dissipation of energy in the locally isotropic turbulence. *Dokl. Akad.*
590 *Nauk SSSR*, **32** (1), 16–18, URL <http://www.jstor.org/stable/51981>.
- 591 Kraus, N. C., A. Lohrmann, and R. Cabrera, 1994: A new acoustic meter for measuring 3D
592 laboratory flows. *Journal of Hydraulic Engineering*, **120**, 406–412.
- 593 Lohrmann, A., R. Cabrera, G. Gelfenbaum, and J. Haines, 1995: Direct measurements of reynolds
594 stress with an acoustic doppler velocimeter. *Current Measurement, 1995.*, *Proceedings of the*
595 *IEEE Fifth Working Conference on*, 205–210, doi:10.1109/CCM.1995.516175.
- 596 Lorke, A., 2007: Boundary mixing in the thermocline of a large lake. *Journal of Geophysical*
597 *Research: Oceans*, **112** (C9), n/a–n/a, doi:10.1029/2006JC004008, c09019.
- 598 Lueck, R. G., and D. Huang, 1999: Dissipation measurement with a moored instrument in a swift
599 tidal channel. *Journal of atmospheric and oceanic technology*, **16**, 1499–1505.
- 600 Lumley, J., and E. Terray, 1983: Kinematics of turbulence convected by a random wave field.
601 *Journal of Physical Oceanography*, **13** (11), 2000–2007.
- 602 McCaffrey, K., B. Fox-Kemper, P. E. Hamlington, and J. Thomson, 2015: Characterization of
603 turbulence anisotropy, coherence, and intermittency at a prospective tidal energy site: Observa-
604 tional data analysis. *Renewable Energy*, **76**, 441–453.
- 605 McMillan, J. M., A. E. Hay, R. G. Lueck, and F. Wolk, 2016: Rates of dissipation of turbulent
606 kinetic energy in a high reynolds number tidal channel. *Journal of Atmospheric and Oceanic*
607 *Technology*, **33** (4), 817–837, doi:10.1175/JTECH-D-15-0167.1.

- 608 MicroStrain, I., 2010: Technical note: Coning and sculling. Tech. Rep. I0019, MicroStrain. URL
609 http://files.microstrain.com/TN-I0019_3DM-GX3-25__Coning_And_Sculling.pdf.
- 610 MicroStrain, I., 2012: *3DM-GX3-15,-25 MIP Data Communications Protocol*. URL <http://files.microstrain.com/3DM-GX3-15-25-MIP-Data-Communications-Protocol.pdf>, retrieved
611 January 2014.
- 612
- 613 Miller, S. D., T. S. Hristov, J. B. Edson, and C. A. Friehe, 2008: Platform motion effects on
614 measurements of turbulence and air-sea exchange over the open ocean. *Journal of Atmospheric*
615 and *Oceanic Technology*, **25** (9), 1683–1694, doi:10.1175/2008JTECHO547.1.
- 616 Morison, J. R., J. W. Johnson, and S. A. Schaaf, 1950: The force exerted by surface waves on
617 piles. *Journal of Petroleum Technology*, **2** (05), 149–154.
- 618 Moum, J., and J. Nash, 2009: Mixing measurements on an equatorial ocean mooring. *Journal of*
619 *Atmospheric and Oceanic Technology*, **26** (2), 317–336.
- 620 Mücke, T., D. Kleinhans, and J. Peinke, 2011: Atmospheric turbulence and its influence on the
621 alternating loads on wind turbines. *Wind Energy*, **14**, 301–316.
- 622 Nash, J. D., L. F. Kilcher, and J. N. Moum, 2009: Structure and composition of a strongly
623 stratified, tidally pulsed river plume. *Journal of Geophysical Research*, **114**, C00B12, doi:
624 10.1029/2008JC005036.
- 625 Nash, J. D., E. Kunze, J. M. Toole, and R. W. Schmitt, 2004: Internal tide reflection and turbulent
626 mixing on the continental slope. *Journal of Physical Oceanography*, **34** (5), 1117–1134, doi:
627 10.1175/1520-0485(2004)034<1117:ITRATM>2.0.CO;2.
- 628 Nortek, 2005: *Vector Current Meter User Manual*. Vangkroken 2, NO-1351 RUD, Norway, h ed.

- 629 Paskyabi, M. B., and I. Fer, 2013: Turbulence measurements in shallow water from a subsurface
630 moored moving platform. *Energy Procedia*, **35**, 307 – 316, doi:10.1016/j.egypro.2013.07.183.
- 631 Perlin, A., and J. N. Moum, 2012: Comparison of thermal variance dissipation rates from moored
632 and profiling instruments at the equator. *Journal of Atmospheric and Oceanic Technology*.
- 633 Polagye, B., and J. Thomson, 2013: Tidal energy resource characterization: methodology and field
634 study in admiralty inlet, Puget Sound, WA (USA). *Proceedings of the Institution of Mechanical
635 Engineers, Part A: Journal of Power and Energy*, **227** (3), 352–367.
- 636 Rippeth, T. P., E. Williams, and J. H. Simpson, 2002: Reynolds stress and turbulent en-
637 ergy production in a tidal channel. *Journal of Physical Oceanography*, **32**, 1242–1251, doi:
638 10.1175/1520-0485(2002)032\$1242:RSATEP\$2.0.CO;2.
- 639 Sreenivasan, K. R., 1995: On the universality of the Kolmogorov constant. *Physics of Fluids*, **7**,
640 2778–2784.
- 641 Stacey, M. T., S. G. Monismith, and J. R. Burau, 1999a: Measurements of reynolds stress
642 profiles in unstratified tidal flow. *J. Geophys. Res.*, **104** (C5), 10 933–10 949, doi:10.1029/
643 1998JC900095.
- 644 Stacey, M. T., S. G. Monismith, and J. R. Burau, 1999b: Observations of turbulence in a partially
645 stratified estuary. *Journal of Physical Oceanography*, **29**, 1950–1970.
- 646 Thomson, J., B. Polagye, V. Durgesh, and M. Richmond, 2012: Measurements of turbulence at
647 two tidal energy sites in Puget Sound, WA. *Journal of Oceanic Engineering*, **37** (3), 363–374,
648 doi:10.1109/JOE.2012.2191656.
- 649 Trowbridge, J. H., 1992: A simple description of the deepening and structure of a stably stratified
650 flow driven by a surface stress. *Journal of Geophysical Research*, **97**, 15 529–15 543.

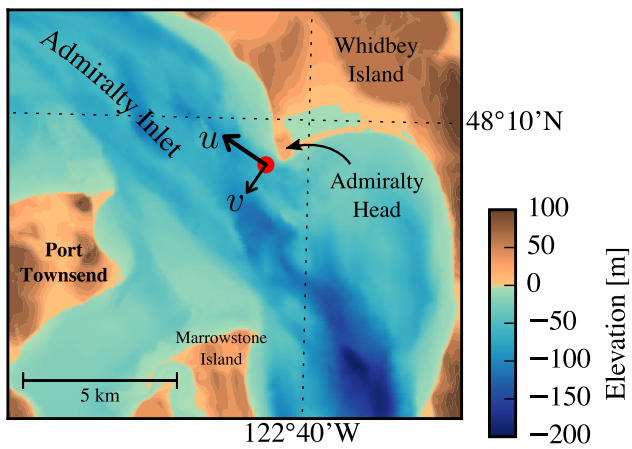
- 651 Trowbridge, J. H., W. R. Geyer, M. M. Bowen, and A. J. I. Williams, 1999: Near-bottom turbu-
652 lence measurements in a partially mixed estuary: turbulent energy balance, velocity structure
653 and along-channel momentum balance. *Journal of Physical Oceanography*, **29**, 3056–3072.
- 654 van der Walt, S., S. C. Colbert, and G. Varoquaux, 2011: The numpy array: A structure for efficient
655 numerical computation. *Computing in Science & Engineering*, **13**, 22–30, doi:10.1109/MCSE.
656 2011.37.
- 657 VanZwieten, J. H., M. N. Egeland, K. D. von Ellenrieder, J. W. Lovenbury, and L. Kilcher, 2015:
658 Experimental evaluation of motion compensated adv measurements for in-stream hydrokinetic
659 applications. *Current, Waves and Turbulence Measurement (CWTM), 2015 IEEE/OES Eleventh*,
660 1–8, doi:10.1109/CWTM.2015.7098119.
- 661 Voulgaris, G., and J. H. Trowbridge, 1998: Evaluation of the acoustic doppler velocimeter (adv)
662 for turbulence measurements. *Journal of Atmospheric and Oceanic technology*, **15**, 272–289.
- 663 Walter, R. K., N. J. Nidzieko, and S. G. Monismith, 2011: Similarity scaling of turbulence spectra
664 and cospectra in a shallow tidal flow. *Journal of Geophysical Research: Oceans*, **116 (C10)**.
- 665 Warner, S. J., P. MacCready, J. N. Moum, and J. D. Nash, 2013: Measurement of tidal form drag
666 using seafloor pressure sensors. *Journal of Physical Oceanography*, **43 (6)**, 1150–1172.
- 667 Wiles, P. J., T. P. Rippeth, J. H. Simpson, and P. J. Hendricks, 2006: A novel technique for
668 measuring the rate of turbulent dissipation in the marine environment. *Geophysical Research
669 Letters*, **33**, 21 608.
- 670 Winkel, D., M. Gregg, and T. Sanford, 1996: Resolving oceanic shear and velocity with the multi-
671 scale profiler. *Journal of Atmospheric and Oceanic Technology*, **13 (5)**, 1046–1072.

672 Wyngaard, J. C., L. Rockwell, and C. A. Friehe, 1985: Errors in the measurement of turbulence
673 upstream of an axisymmetric body. *Journal of Atmospheric and Oceanic Technology*, **2** (4),
674 605–614.

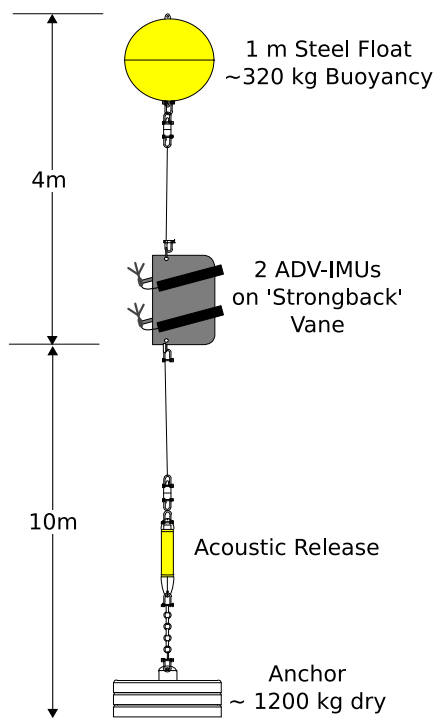
675 Zhang, Y., K. Streitlien, J. G. Bellingham, and A. B. Baggeroer, 2001: Acoustic doppler ve-
676 locimeter flow measurement from an autonomous underwater vehicle with applications to deep
677 ocean convection. *Journal of Atmospheric and Oceanic Technology*, **18** (12), 2038–2051, doi:
678 [10.1175/1520-0426\(2001\)018<2038:ADVFMF>2.0.CO;2](https://doi.org/10.1175/1520-0426(2001)018<2038:ADVFMF>2.0.CO;2).

679 LIST OF FIGURES

680	Fig. 1.	Bathymetry of Admiralty Inlet near Port Townsend, Washington, U.S.A. (Finlayson 2005). The red dot indicates the location of all measurements. The positive u direction is the direction of ebb flow (thick arrow originating from red dot), and positive v is away from Admiralty Head (smaller arrow).	35
684	Fig. 2.	Schematic diagram of the TTM; not to scale. A pop-up buoy for anchor recovery is not shown, for simplicity.	36
686	Fig. 3.	TTM components on the deck of the R/V Jack Robertson. The TTM includes two ADVs, with pressure cases mounted on opposite sides of the fin. The anchor stack includes a pop-up buoy for retrieval. The green arrow indicates the vector from the IMU to the ADV head (face of the transmit transducer).	37
690	Fig. 4.	Top: Alex DeKlerk checks to ensure that the SMB buoy is properly fastened to its anchor; the RDI workhorse ADP can be seen in the rear instrument bay. A bridle is draped across the top of the buoy for deployment and recovery, and a small marker buoy fastened to the tail is useful during recovery. Bottom: a close-up of the SMB buoy with the ADV head and the top of its pressure case. The green arrow indicates the vector from the IMU to the ADV head.	38
696	Fig. 5.	The turbulence platform showing details of the ADV head and pressure case configuration. The green arrow indicates the vector from the IMU to the ADV head. The head cable was taped out of the way beneath the sounding weight tail fins shortly after taking this photo.	39
699	Fig. 6.	The spectral noise levels of rotational velocity ($S\{\mathbf{n}_\omega\}$, yellow) and translational velocity ($S\{\mathbf{n}_a\}$, black) estimated from an ADV-IMU resting motionless on a table. Solid and dashed lines indicate the horizontal and vertical components, respectively, of $S\{\mathbf{n}_a\}$ and $S\{\mathbf{u}_{low}\}$. The \mathbf{n}_a signals are unfiltered (black), and high-pass filtered at 0.03 Hz (blue) and 0.3 Hz (red); vertical dotted lines indicate the filter frequency. Green lines are an estimate of \mathbf{u}_{low} for the TTM. Grey horizontal lines indicate the horizontal (solid) and vertical (dashed) ADV noise levels. The shaded region indicates the range of $S\{u\}$ presented in the next section.	40
706	Fig. 7.	Motion-corrected velocity spectra, $S\{\mathbf{u}\}$, for a range of high-pass filter frequencies: $f_a = 0.3$ Hz (thin red), 0.03 Hz (blue), and 0.003 Hz (thick black). The vertical dashed-dotted lines indicate the filter frequency. The thick grey line is $S\{\mathbf{u}_h\}$ for $f_a = 0.003$ Hz. The data are from the June 2014 TTM deployment when $2.0 < \bar{u} < 2.5 \text{ ms}^{-1}$.	41
710	Fig. 8.	Time series of tidal velocity in June 2012 at Admiralty Head from ADV-IMU measurements (black), and an ADP on the anchor (red). Note that the vertical scale on the three axes vary by more than an order of magnitude; the small ticks in A and B are equivalent to the ticks in C.	42
714	Fig. 9.	Turbulence spectra from the June 2014 TTM deployment. Each column is for a range of streamwise velocity magnitudes (indicated at top, in ms^{-1}). The rows are for each component of velocity (indicated at far right). The uncorrected spectra are black, the corrected spectra are blue, and the spectra of ADV head motion is red (also indicated in the legend). The vertical red dotted line indicates f_a for estimating \mathbf{u}_h ; below this frequency $S\{\mathbf{u}_h\}$ is plotted as a dashed line. Diagonal black dotted lines indicate a $f^{-5/3}$ slope. The cyan line in the first and last rows indicates the semi-empirical Kaimal spectrum for the measured values of u_* and \bar{U} . The number of spectral ensembles, N , in each column is indicated in the top row.	43



752 FIG. 1. Bathymetry of Admiralty Inlet near Port Townsend, Washington, U.S.A. (Finlayson 2005). The red
 753 dot indicates the location of all measurements. The positive u direction is the direction of ebb flow (thick arrow
 754 originating from red dot), and positive v is away from Admiralty Head (smaller arrow).



755 FIG. 2. Schematic diagram of the TTM; not to scale. A pop-up buoy for anchor recovery is not shown, for
 756 simplicity.



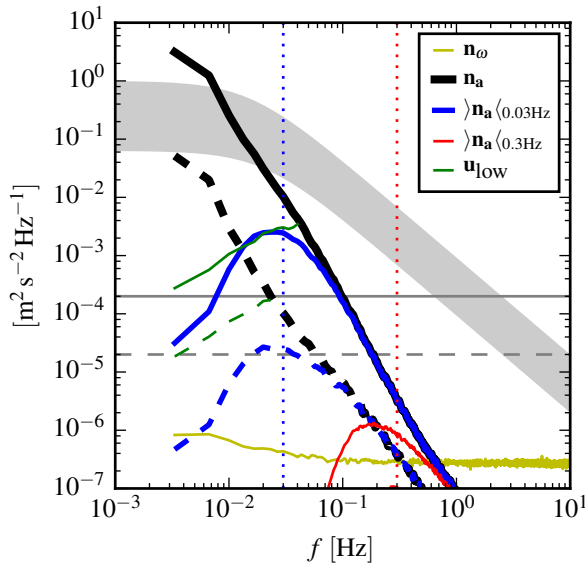
757 FIG. 3. TTM components on the deck of the R/V Jack Robertson. The TTM includes two ADVs, with
758 pressure cases mounted on opposite sides of the fin. The anchor stack includes a pop-up buoy for retrieval. The
759 green arrow indicates the vector from the IMU to the ADV head (face of the transmit transducer).



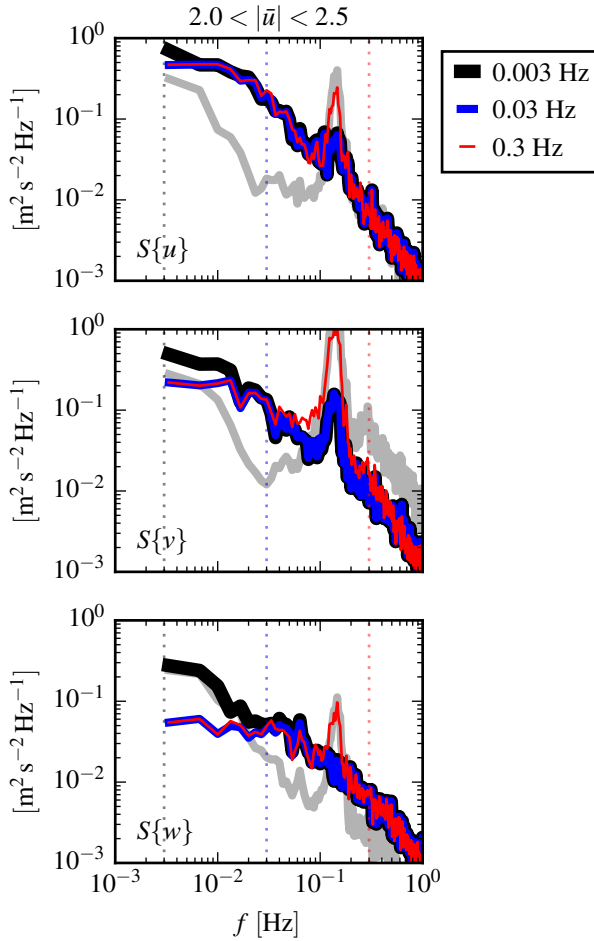
760 FIG. 4. Top: Alex DeKlerk checks to ensure that the SMB buoy is properly fastened to its anchor; the
 761 RDI workhorse ADP can be seen in the rear instrument bay. A bridle is draped across the top of the buoy for
 762 deployment and recovery, and a small marker buoy fastened to the tail is useful during recovery. Bottom: a
 763 close-up of the SMB buoy with the ADV head and the top of its pressure case. The green arrow indicates the
 764 vector from the IMU to the ADV head.



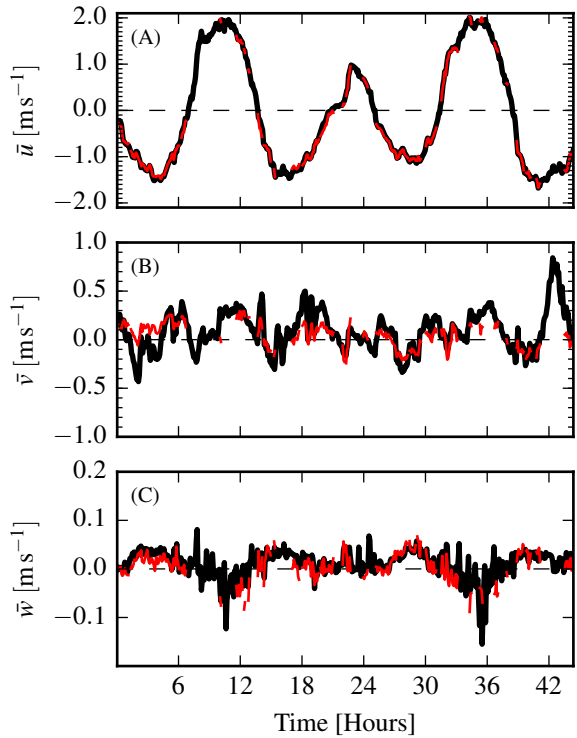
765 FIG. 5. The turbulence platform showing details of the ADV head and pressure case configuration. The green
766 arrow indicates the vector from the IMU to the ADV head. The head cable was taped out of the way beneath the
767 sounding weight tail fins shortly after taking this photo.



768 FIG. 6. The spectral noise levels of rotational velocity ($S\{\mathbf{n}_\omega\}$, yellow) and translational velocity ($S\{\mathbf{n}_a\}$,
 769 black) estimated from an ADV-IMU resting motionless on a table. Solid and dashed lines indicate the horizontal
 770 and vertical components, respectively, of $S\{\mathbf{n}_a\}$ and $S\{\mathbf{u}_{\text{low}}\}$. The \mathbf{n}_a signals are unfiltered (black), and high-
 771 pass filtered at 0.03 Hz (blue) and 0.3 Hz (red); vertical dotted lines indicate the filter frequency. Green lines are
 772 an estimate of \mathbf{u}_{low} for the TTM. Grey horizontal lines indicate the horizontal (solid) and vertical (dashed) ADV
 773 noise levels. The shaded region indicates the range of $S\{u\}$ presented in the next section.



774 FIG. 7. Motion-corrected velocity spectra, $S\{\mathbf{u}\}$, for a range of high-pass filter frequencies: $f_a = 0.3$ Hz (thin
 775 red), 0.03 Hz (blue), and 0.003 Hz (thick black). The vertical dashed-dotted lines indicate the filter frequency.
 776 The thick grey line is $S\{\mathbf{u}_h\}$ for $f_a = 0.003$ Hz. The data are from the June 2014 TTM deployment when
 777 $2.0 < |\bar{u}| < 2.5 \text{ ms}^{-1}$.



778 FIG. 8. Time series of tidal velocity in June 2012 at Admiralty Head from ADV-IMU measurements (black),
 779 and an ADP on the anchor (red). Note that the vertical scale on the three axes vary by ~~more than~~ an order of
 780 magnitude; the small ticks in A and B are equivalent to the ticks in C.

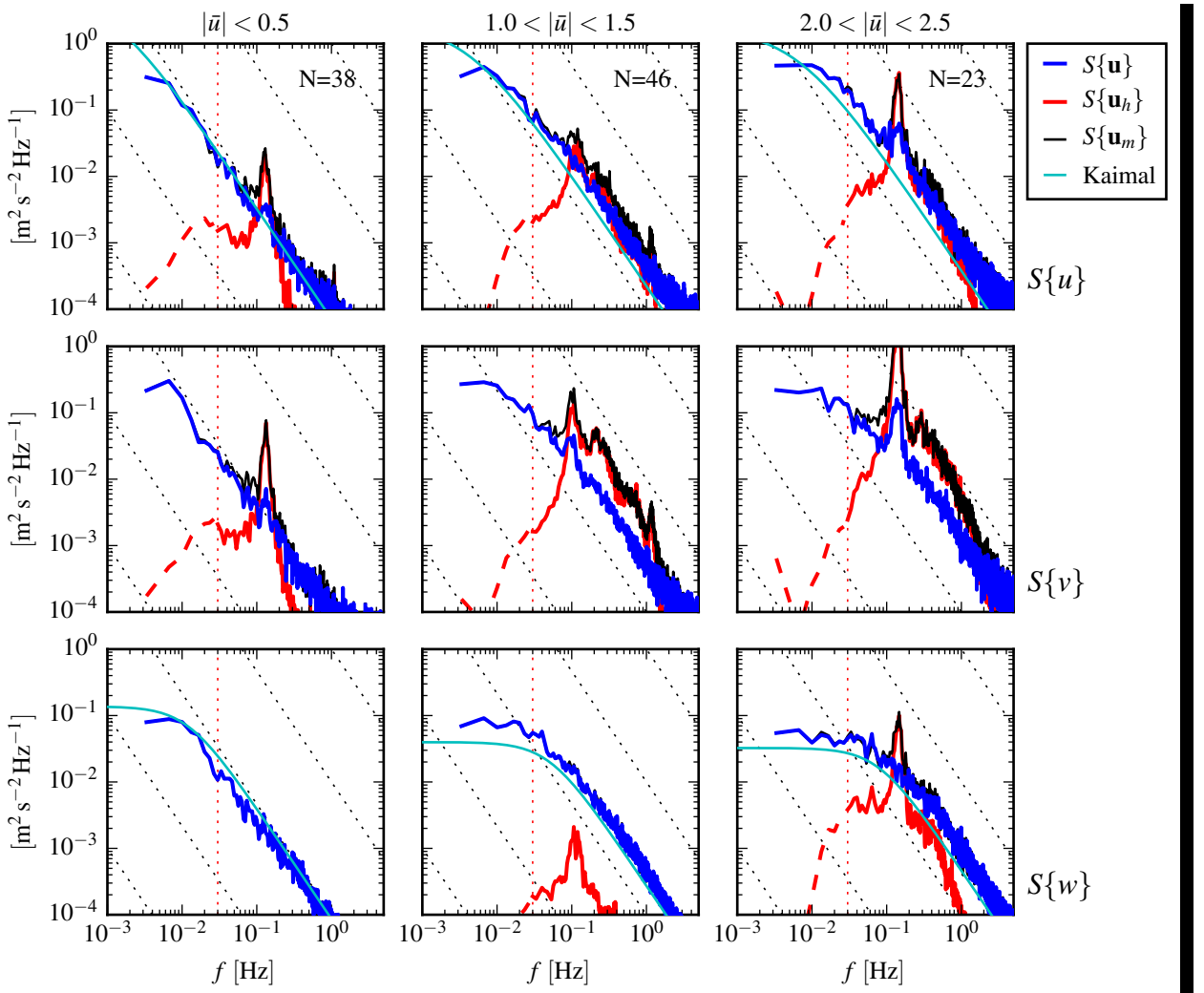
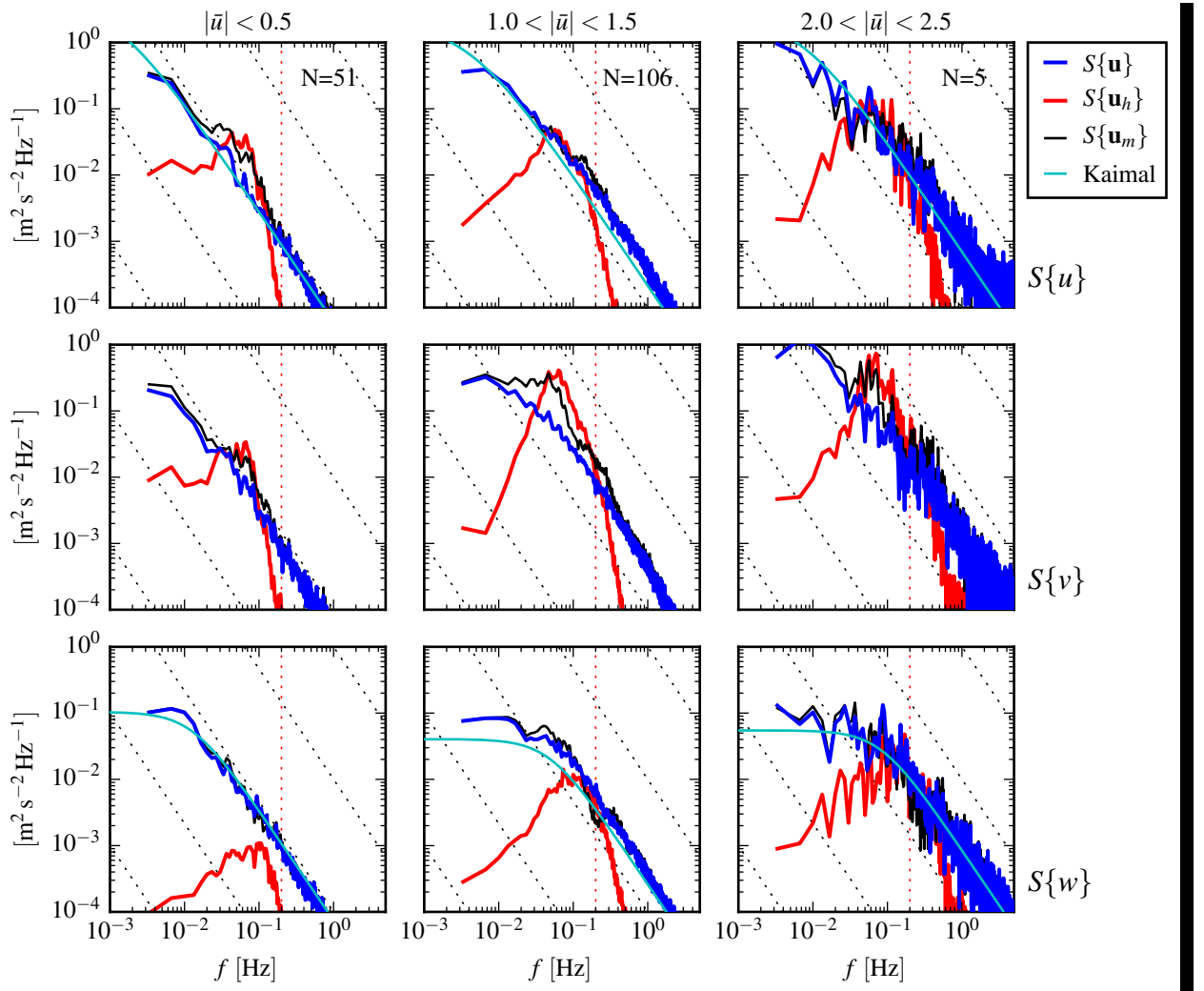
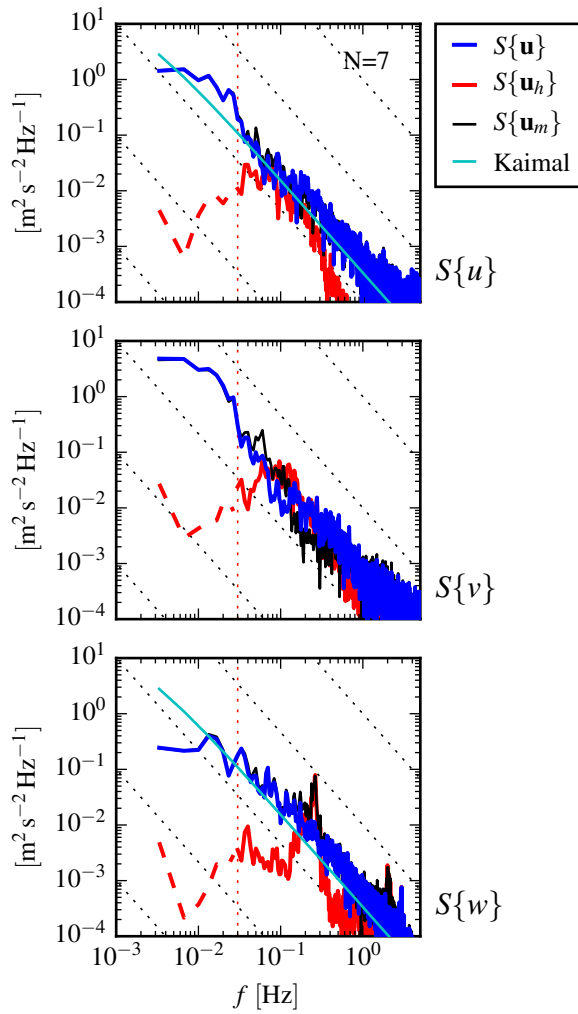


FIG. 9. Turbulence spectra from the June 2014 TTM deployment. Each column is for a range of streamwise velocity magnitudes (indicated at top, in m s^{-1}). The rows are for each component of velocity (indicated at far right). The uncorrected spectra are black, the corrected spectra are blue, and the spectra of ADV head motion is red (also indicated in the legend). The vertical red dotted line indicates f_a for estimating \mathbf{u}_h ; below this frequency $S\{\mathbf{u}_h\}$ is plotted as a dashed line. Diagonal black dotted lines indicate a $f^{-5/3}$ slope. The cyan line in the first and last rows indicates the semi-empirical Kaimal spectrum for the measured values of u_* and \bar{U} . The number of spectral ensembles, N , in each column is indicated in the top row.



788 FIG. 10. Turbulence spectra from the SMB. The axes layout and annotations are identical to Figure 9, except
 789 that $S\{\mathbf{u}_h\}$ is plotted as a solid line at all frequencies because it is measured at all frequencies.



790 FIG. 11. Turbulence spectra from the turbulence torpedo during a 35-minute period when the mean velocity
 791 was 1.3 m/s . Annotations and line colors are identical to Figure 9.

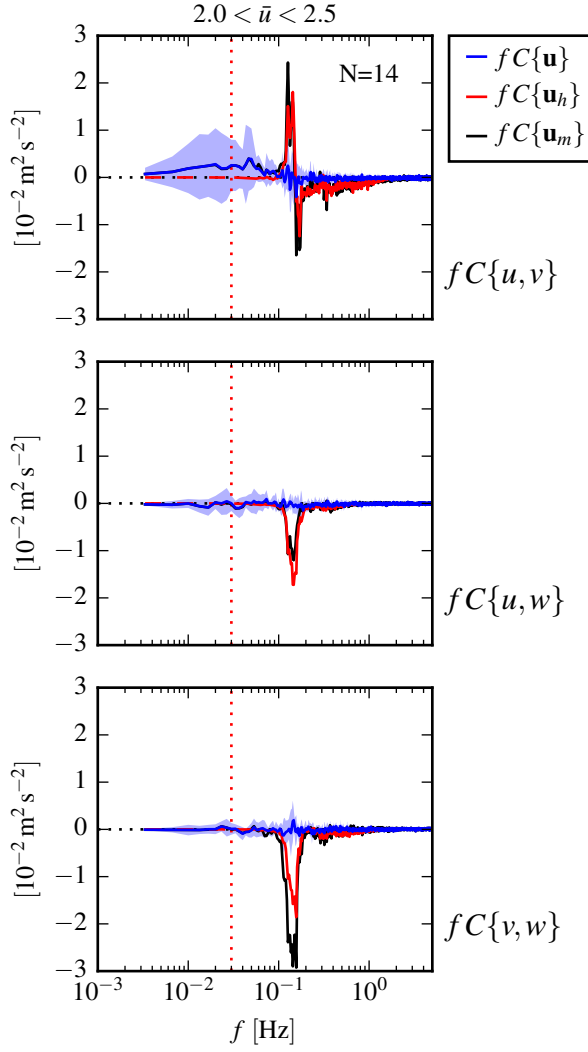
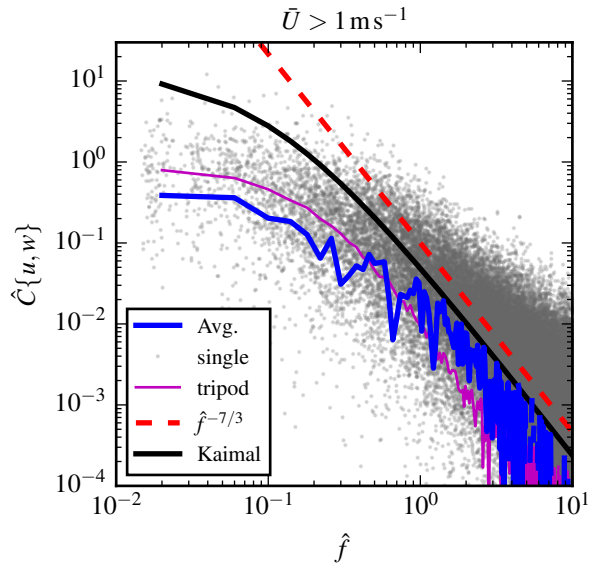


FIG. 12. Variance preserving cross-spectra between components of \mathbf{u} (blue), \mathbf{u}_h (red), and \mathbf{u}_m (black) from the June 2014 TTM deployment. The upper row is $f\text{-}C\{\mathbf{u}, \mathbf{v}\} fC\{\mathbf{u}, \mathbf{v}\}$, the middle row is $f\text{-}C\{\mathbf{u}, \mathbf{w}\} fC\{\mathbf{u}, \mathbf{w}\}$, and the bottom row is $f\text{-}C\{\mathbf{v}, \mathbf{w}\} fC\{\mathbf{v}, \mathbf{w}\}$ (also indicated at right). Note that these cross-spectra are between components of a velocity vector (e.g., \mathbf{u}), not between different vectors (i.e., not between \mathbf{u} and \mathbf{u}_m). N is the number of spectral ensembles in this average, i.e. when $2 < |\mathbf{u}| < 2.5 \text{ [ms}^{-1}]$. The light blue shading indicates one standard deviation of $f\text{-}C\{\mathbf{u}\} fC\{\mathbf{u}\}$.



798 FIG. 13. Non-dimensional cross-spectra of motion corrected velocity, $\hat{C}\{u, w\}$, on a log-log scale. The average
 799 over $\Delta \hat{f} = 0.04$ bins is shown in blue, and single points are grey (negative values not shown). The semi-empirical
 800 Kaimal et al. (1972) form is shown as a thick black line, and the red dashed line indicates a $\hat{f}^{-7/3}$ slope. Cross-
 801 spectral estimates from measurements from a fixed ‘tripod’ are in purple.

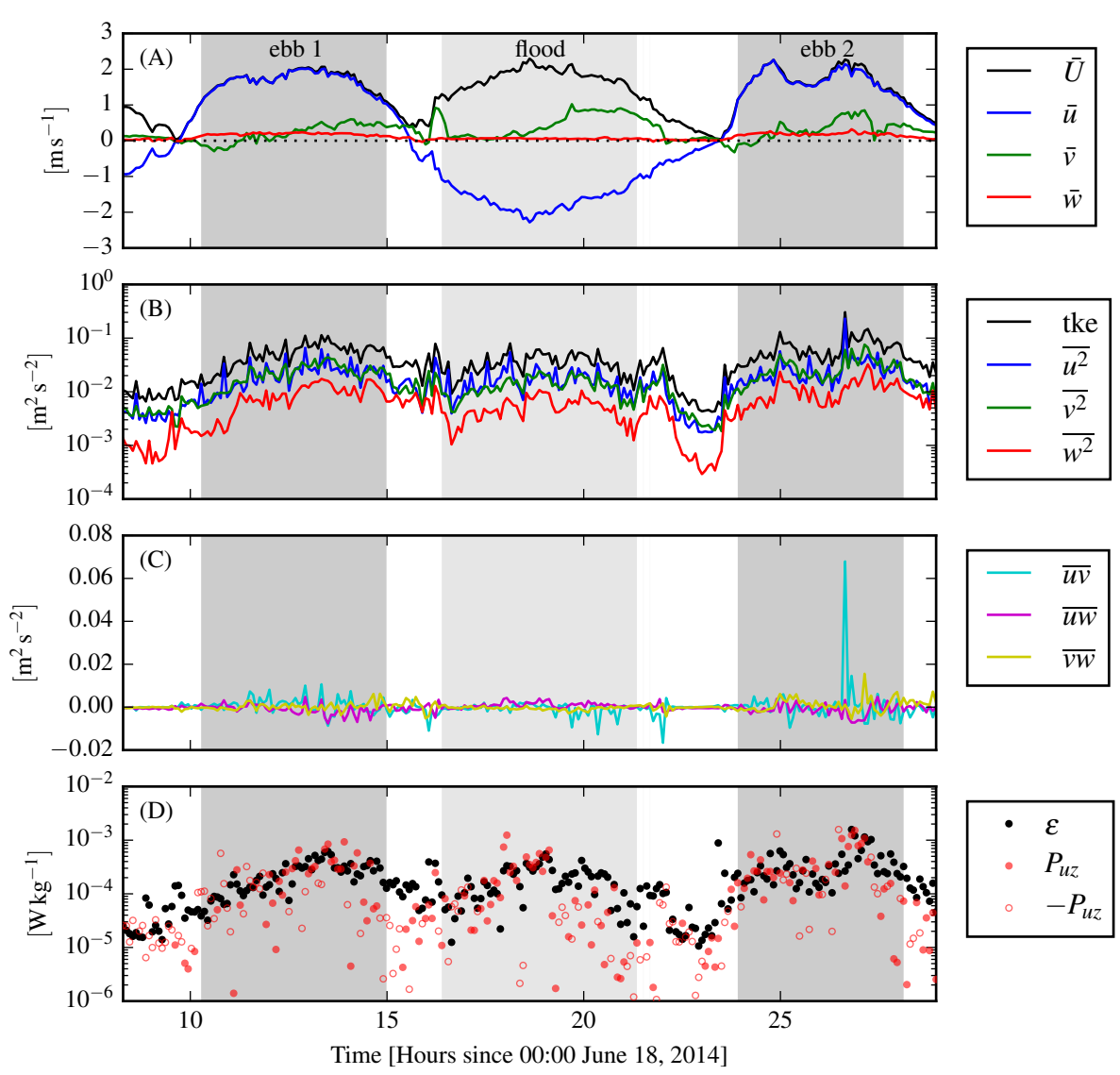
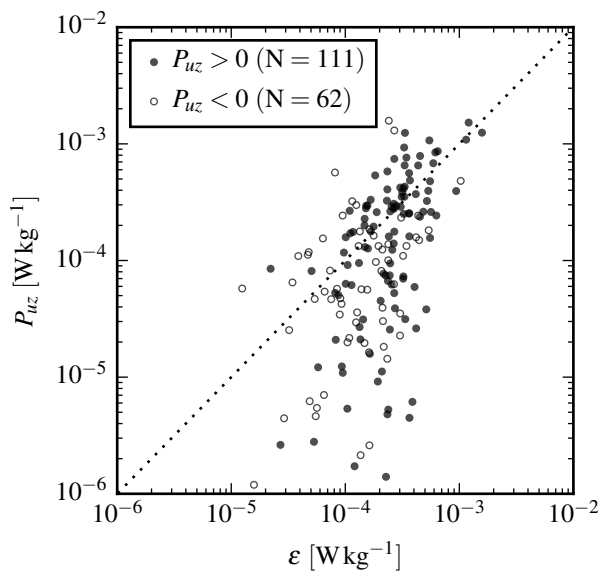


FIG. 14. Time series of mean velocities (A), turbulence energy and its components (B), Reynold's stresses (C), and turbulence dissipation rate (D) measured by the TTM during the June 2014 deployment. Shading indicates periods of ebb ($\bar{u} > 1.0 \text{ ms}^{-1}$, grey) and flood ($\bar{u} < -1.0 \text{ ms}^{-1}$, lighter grey).



805 FIG. 15. P_{uz} vs. ϵ during the June 2014 TTM deployment for values of $|u| > 1$ m/s. Values of negative
806 production are indicated as open circles.

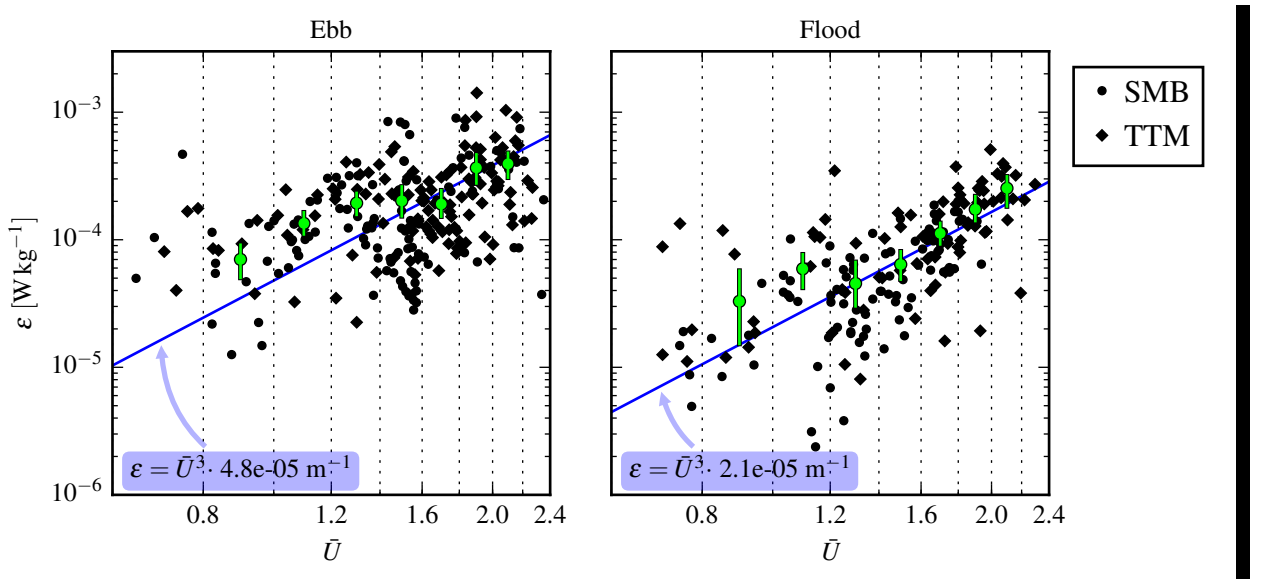


FIG. 16. A log-log plot of ε vs. \bar{U} for the June 2014 TTM (diamonds) and May 2015 SMB (dots) deployments, during ebb (left) and flood (right). Black points are 5-minute averages. Green dots are mean values within speed bins of 0.2 m s^{-1} width that have at least 10 points (50 minutes of data); their vertical bars are 95% bootstrap confidence intervals. The blue line shows a \bar{U}^3 slope, wherein the proportionality constant (blue box) is calculated by taking the log-space mean of ε/\bar{U}^3 .